

Article

$C_{0.3}N_{0.7}Ti$ -SiC Toughed Silicon Nitride Hybrids with Non-Oxide Additives Ti_3SiC_2

Heng Luo ^{1,*} , Chen Li ¹, Lianwen Deng ¹, Yang Li ², Peng Xiao ² and Haibin Zhang ³

¹ School of Physics and Electronics, Central South University, Changsha 410083, China; li-richard@foxmail.com (C.L.); denglw@csu.edu.cn (L.D.)

² State Key Laboratory of Powder Metallurgy, Central South University, Changsha 410083, China; liyang_csu@126.com (Y.L.); xiaopengcsu@csu.edu.cn (P.X.)

³ Innovation Research Team for Advanced Ceramics, Institute of Nuclear Physics and Chemistry, China Academy of Engineering Physics, Mianyang 621900, China; hbzhang@caep.cn

* Correspondence: luohengcsu@csu.edu.cn

Received: 28 February 2020; Accepted: 18 March 2020; Published: 20 March 2020



Abstract: In situ grown $C_{0.3}N_{0.7}Ti$ and SiC, which derived from non-oxide additives Ti_3SiC_2 , are proposed to densify silicon nitride (Si_3N_4) ceramics with enhanced mechanical performance via hot-press sintering. Remarkable increase of density from 79.20% to 95.48% could be achieved for Si_3N_4 ceramics with 5 vol.% Ti_3SiC_2 when sintered at 1600 °C. As expected, higher sintering temperature 1700 °C could further promote densification of Si_3N_4 ceramics filled with Ti_3SiC_2 . The capillarity of decomposed Si from Ti_3SiC_2 , and in situ reaction between nonstoichiometric TiC_x and Si_3N_4 were believed to be responsible for densification of Si_3N_4 ceramics. An obvious enhancement of flexural strength and fracture toughness for Si_3N_4 with x vol.% Ti_3SiC_2 ($x = 1\sim 20$) ceramics was observed. The maximum flexural strength of 795 MPa for Si_3N_4 composites with 5 vol.% Ti_3SiC_2 and maximum fracture toughness of $6.97\text{ MPa}\cdot\text{m}^{1/2}$ for Si_3N_4 composites with 20 vol.% Ti_3SiC_2 are achieved via hot-press sintering at 1700 °C. Pull out of elongated Si_3N_4 grains, crack bridging, crack branching and crack deflection were demonstrated to dominate enhance fracture toughness of Si_3N_4 composites.

Keywords: Ti_3SiC_2 ; Si_3N_4 ; mechanical properties; fracture toughness

1. Introduction

Although several alternatives of structural ceramics have been proposed, silicon nitride (Si_3N_4)-based ceramics remain competitive due to their superior properties, involving high strength and hardness at elevated temperatures, high resistance to oxidation and chemical attack, low coefficient of tribological friction and thermal expansion, and low dielectric permittivity, etc. [1–10]. As important multifunctional materials, Si_3N_4 ceramics have found wide range of successful application towards gas turbine engine components [10–14], cutting tools [11,15], radomes [2], and even integrated circuit [16,17], optical devices [18,19], etc.

However, due to the high degree of covalent bonding, Si_3N_4 -based ceramics are very difficult to densify through the solid-state sintering process. Therefore, effective approaches to ensure rapid consolidation and high mechanical performance of Si_3N_4 -based ceramics are actively being explored, including gas pressure sintering (GPS) [11], hot-pressing sintering (HPS) [20–26], hot isostatic pressing sintering (HIP) [27], spark plasma sintering (SPS) [26,28,29], and microwave sintering [1,30], etc. However, considering the requirement of high gas pressures for gas pressure sintering and extra current devices for SPS with a significantly higher furnace costs, HPS allows the dense and complex-shaped parts with medium cost [2]. Previous considerable efforts have demonstrated that fully dense Si_3N_4 ceramics with superior strength could be achieved through liquid phase sintering by

addition of rare-earth oxides to promote mass transport and accelerate the rate of $\alpha - \beta$ transformation, most notably the rare-earth oxides involving Y_2O_3 [4,31,32]. A combination of various rare-earth oxides and other metallic oxides, such as Y_2O_3 , La_2O_3 , Nd_2O_3 , Sm_2O_3 , Yb_2O_3 , Lu_2O_3 , Al_2O_3 , and MgO , also are effective sintering aids to densify Si_3N_4 [25,30,32–35].

Nevertheless, these oxides additives crystallized to intergranular glassy phase in the cooling stage [31], which deteriorate the high-temperature performance of the ceramics such as creep and high-temperature strength due to the relative low eutectic temperature [32,36]. As a result of the early interest in hot-pressed Si_3N_4 ceramics as a high-temperature gas turbine material, attention was directed to high-temperature strength and creep resistance. Therefore, it is quite essential to explore novel heat-resistant sintering aids for high-performance Si_3N_4 ceramics from new view point.

The last two decades have been witness to the dramatic development on MAX phase cermets with the hexagonal symmetry due to their unique combination of characteristics of both ceramics and metals (M is an early transition metal, A is a group A element, X is either carbon and/or nitrogen), especially the layered ternary carbide titanium aluminum carbide (Ti_3AlC_2) and titanium silicon carbide (Ti_3SiC_2) [37–39]. The crystal structure of these MAX cermets can be described by alternately stacking of TiC_6 and Al/Si atomic planes. The unique combination of excellent properties of Ti_3AlC_2 or Ti_3SiC_2 , including high melting point, high hardness, high elastic modulus, good thermal and electrical conductivity, and considerable chemical stability, make them to be fascinating candidates for various application. Moreover, elemental metal powder-derived MAX materials have demonstrated to be effective reinforcement in TiB_2 [40–42], Al_2O_3 [43–45] composites with enhanced mechanical properties by in situ reaction. More recently, as explicated in our previous work [46–50], titanium aluminum carbide (Ti_3AlC_2) was chosen as an effective sintering aid to effectively densify B_4C ceramics with enhanced sintering ability and mechanical performance simultaneously. High hardness and toughness values of 28.5 GPa and $7.02 \text{ MPa}\cdot\text{m}^{1/2}$ respectively were achieved for B_4C composites sintered with 20 vol.% Ti_3AlC_2 at 1900 °C. The mechanisms of the enhanced sinterability of high-performance ceramics in previous works [1,10,46–50] could be classified into two aspects: Firstly, the decomposed metals from Ti_3SiC_2 or Ti_3AlC_2 at high-temperature can form liquid phase which promote sintering effectively. Secondly, in situ reaction sintering between matrix and titanium carbon compound would also promote densification and mechanical performance. The main competitive advantage of MAX aids is considered to be formation of reaction bonding between Si_3N_4 matrix and aids, rather than intergranular glassy phase. Motivated by such an idea [46–50], these non-oxides cermets are highly expected to play a multifunctional role in densification and enhancement of mechanical properties of Si_3N_4 ceramics.

It is also noteworthy that Al decomposed from Ti_3AlC_2 and residual O originated from raw Si_3N_4 powders would be dissolved into Si_3N_4 grains during high-temperature sintering procedure, which is harmful to the purity and thermal performance of Si_3N_4 -based ceramics. As Y. Zhou et al. illustrated [51], a tendency of decreasing fracture toughness with increasing Al dopant could be observed. Moreover, even the 0.4 wt.% concentration of Al would lead to a drastically reduce of thermal conductivity by 36.9% (from 91.9 to $58.0 \text{ W}\cdot\text{m}^{-1}\cdot\text{K}^{-1}$) for Si_3N_4 ceramics. Therefore in this work, Ti_3SiC_2 were introduced to densify Si_3N_4 ceramics in order to demonstrate that it provided any advantages over the rare-earth oxide system. Besides, the effect of Ti_3SiC_2 volume fraction on the microstructure, hardness, flexural strength and fracture toughness was also studied. It is believed that Ti_3SiC_2 or other members of MAX family would lead to new scientific and technological data providing new insight into functionalization of Si_3N_4 ceramics.

2. Experimental Procedure

2.1. Preparation of Samples

Commercially available α - Si_3N_4 powder (purity > 93%, $d_{50} = 0.7 \mu\text{m}$, Jinshenghao New Materials Co. Ltd., Anyang, China) was used as a starting material. As a novel sintering aid, Ti_3SiC_2 powders

($d_{50} = 5 \mu\text{m}$, purity > 98%) were kindly provided by Forsman Scientific Co., Ltd., Beijing, China. To investigate the effect of Ti_3SiC_2 content on the mechanical properties, experiments were conducted with various amounts of Ti_3SiC_2 powders (1 to 20 vol.%) embedded in $\alpha\text{-Si}_3\text{N}_4$ powders. To ensure the homogeneity of the mixed powders, $\alpha\text{-Si}_3\text{N}_4$ with x vol.% Ti_3SiC_2 powders ($x = 1\sim 20$) were wet ball-milled for 10 h by using ethanol as ball-milling media. The substance was dried at 80°C , and sieved with a filter with a mesh size of $63 \mu\text{m}$, then placed in a graphite die coated with BN powder to avoid reaction between the powder and graphite die. Hot-press (HP) sintering was performed on vacuum hot press sintering furnace (ZT-63-21Y, Shanghai Chenhua Technology Co., Ltd., Shanghai, China) with ramp of $10^\circ\text{C}/\text{min}$ 1600°C and 1700°C for 90 min in flowing nitrogen under 30 MPa uniaxial pressure during the whole cycle. After natural cooling to room temperature inside furnace, samples were polished and ultrasonic cleaned before characterization. For comparison, $\alpha\text{-Si}_3\text{N}_4$ powders with 2 wt.% Alumina (Al_2O_3 , AR, Sinopharm Chemical Reagent Co., Ltd., Shanghai, China) and 5 wt.% yttria (Y_2O_3 , AR, Sinopharm Chemical Reagent Co., Ltd., Shanghai, China) were hot-pressed at the same sintering condition.

2.2. Characterizations

Before microstructure and mechanical performance characterizations, all hot-pressed samples with diameter of 50 mm were cut into bars and cuboids with help of inside diameter slicer. To reduce surface roughness of samples and guarantee sufficient experimental precision, the abrasive SiC papers with grit size of P320, P600, P1200 and P2000 were used in chronological order during the polishing process. Final manual polishing was carried out with polishing cloth containing alumina suspension with particle size $0.3 \mu\text{m}$. The bulk density of each sample was determined according to the Archimedes principle in distilled water. X-ray Diffraction (XRD) patterns were recorded on X'pert PRO (PANalytical B.V., Almelo, Netherlands). Phase identification and quantitative analysis were performed on MDI Jade software (version 6.0, MDI, Livermore, CA, USA) according to Rietveld method. The microstructures of polished surfaces and fracture surfaces were observed using scanning electron microscopy (SEM, Nova NanoSEM 230, FEI Company, Hillsboro, OR, USA) with an energy dispersive X-ray (EDX) analyzer. The Vickers hardness was performed on micro hardness tester (VTD 512, Beijing Weiwei Technology Co., LTD, Beijing, China) under load of 9.8 N with a dwell time of 10 s, and determined by the Vickers diamond indentation method using the following equation:

$$H_V = 0.102 \frac{F}{S} = 0.102 \frac{2F \sin \frac{136}{2}}{d^2} = 0.1891 \frac{F}{d^2} \quad (1)$$

where P is the indentation load on the polished surface and d is the average diagonal length of the Vickers indentation. For accuracy, 11 Vickers indentations on each specimen were applied. After indentation, the microstructures were immediately observed by optical microscopy (ECLISPE LV150N, Tokyo, Japan). As a simple way of estimating toughness, indentation techniques were applied from observed corner cracks and calculated Vickers hardness using the Anstis equation:

$$K_{IC} = 0.016 \left(\frac{E}{H_V} \right)^{\frac{1}{2}} \left(\frac{P}{c^{\frac{3}{2}}} \right) \quad (2)$$

where E is the Young's modulus and c is the half-length of cracks formed by the indentation. According to the international standard of test method for flexural strength of fine monolithic ceramics at room temperature which described in ISO 14704-2000, three-point flexural strength of specimens with size of $3 \text{ mm} \times 4 \text{ mm} \times 36 \text{ mm}$ was performed on the mechanical testing machine (Instron 3369, INSTRON Corporation, Norwood, MA, USA) at a cross head speed of $0.5 \text{ mm}/\text{min}$.

3. Results and Discussion

Figure 1 illustrates the density of Ti_3SiC_2 filled Si_3N_4 ceramics as a function of Ti_3SiC_2 volume fraction. For Si_3N_4 ceramics which HP sintered at 1600 °C without aids, the density is only 2.58 $\text{g}\cdot\text{cm}^{-3}$. Partial densification may be attributed to the residual SiO_2 liquid phase during firing at high-temperature which always present on Si_3N_4 powder particles. A remarkable increase to 3.11 $\text{g}\cdot\text{cm}^{-3}$ could be observed for Si_3N_4 ceramics filled with only 5 vol.% Ti_3SiC_2 when sintered at the same temperature. The enhanced density is even more noticeable than the Si_3N_4 ceramics with 7 wt.% $\text{Y}_2\text{O}_3\text{-Al}_2\text{O}_3$ aids. These observed results demonstrate Ti_3SiC_2 to be a effective sintering aid to densify Si_3N_4 ceramics. However, further increase in Ti_3SiC_2 content dose not bring any appreciable consolidation.

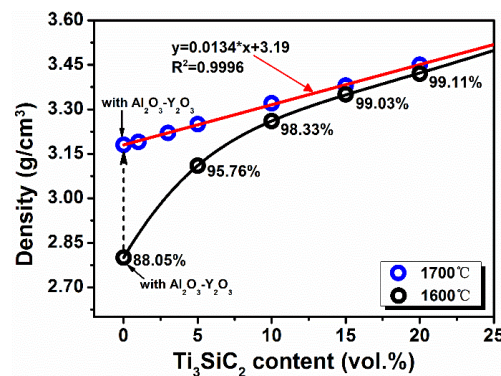
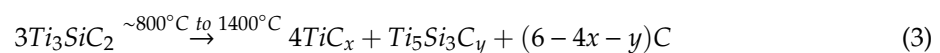


Figure 1. Density of Si_3N_4 ceramics as a function of Ti_3SiC_2 content.

As expected, higher sintering temperature 1700 °C could further promote densification of Si_3N_4 ceramics filled with Ti_3SiC_2 . Besides, experimental points are inclined to distribute on a straight line with coefficient of determination (R^2) above 0.99. To investigate the composition evolution after sintering, XRD patterns of Si_3N_4 ceramics filled with different volume fraction of Ti_3SiC_2 sintered at 1600 and 1700 °C, as well as 7 wt.% ($\text{Al}_2\text{O}_3\text{-Y}_2\text{O}_3$) densified Si_3N_4 ceramics are shown in Figure 2. As seen in Figure 2a, both α and β phase of Si_3N_4 could be detected when sintering temperature is 1600 °C, which suggests only a partial transformation of α phase to the more stable β phase. In contrast, when further improving sintering temperature to 1700 °C, all diffraction peaks of $\alpha\text{-Si}_3\text{N}_4$ phase disappear (see in Figure 2b). This completely transformation of α to $\beta\text{-Si}_3\text{N}_4$ phase is believed to be essential to the enhancement of densification and mechanical performance [1,52].

Another important feature should be noted here is that the characteristic diffraction peaks of the raw Ti_3SiC_2 powder nearly disappear completely after sintering. This could be ascribed to the fact that Ti_3SiC_2 powder is thermal stable up to ~800 °C, and the following reaction can be responsible for the decomposition of Ti_3SiC_2 [53]:



where the value of x ranges from 0.6 to 0.8 and $y \leq 1$. Besides, the TiC_x phase appears to result in more rapid deterioration of the Ti_3SiC_2 phase. Also noted that the decomposition usually accomplished with decomposition of Ti_3SiC_2 to form nonstoichiometric TiC_x and gaseous Si, as demonstrated previously [54]:



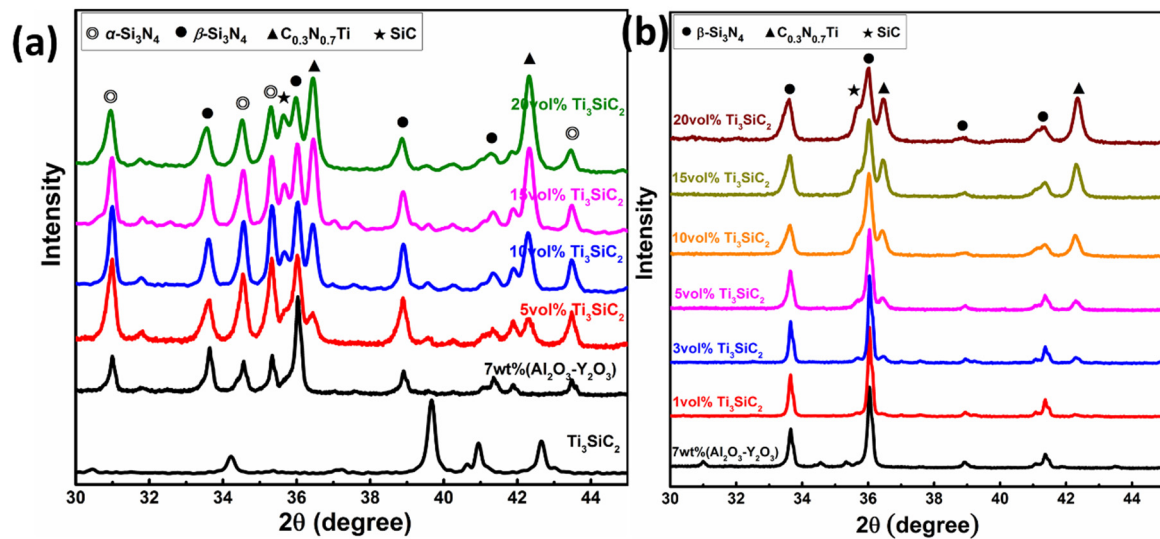
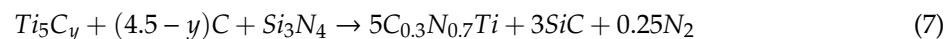
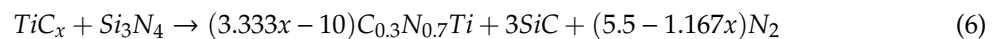
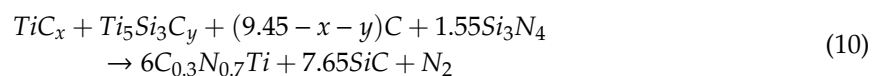


Figure 2. XRD patterns of Ti_3SiC_2 doped Si_3N_4 ceramics sintered at (a) 1600 and (b) 1700 °C.

The Si is believed to be act as lubricating phase between Si_3N_4 grains to promote densification of Si_3N_4 ceramics through capillarity. Meanwhile, nitriding of TiC_x which originated from interatomic diffusion of C and N [10] during high-temperature sintering process would lead to the formation of new phase $C_{0.3}N_{0.7}Ti$. In addition, the residual Si would further react with nitrogen to form Si_3N_4 [55–57]. On the other hand, further heating during insulation stage will result in the likely loss of gaseous silicon. Therefore, it is reasonable to assume that the decomposition products of Ti_3SiC_2 would further react with Si_3N_4 through diffusion of C and N according to the following reactions:



or



It is reasonable to claim that the in situ reaction is responsible for the additional characteristic diffraction peaks of $C_{0.3}N_{0.7}Ti$ and SiC in XRD patterns.

Furthermore, detailed refinement parameters by means of Rietveld method are summarized in Table 1. Detailed refinement parameters, including weight fraction and R factor, of Ti_3SiC_2 doped Si_3N_4 ceramics are illustrated in Figures S1–S6 (see in Supplementary Materials). Obviously, the weight fraction of both $C_{0.3}N_{0.7}Ti$ (Fm-3m, PDF# 42-1448) and moissanite-3C SiC (F-43m, PDF# 29-1129) are inclined to increase with Ti_3SiC_2 content, which in turn confirms the in situ densification sintering mechanism discussed above. In addition, theoretical density could be derived with help of Rietveld method. Results have shown that nearly full densification for Ti_3SiC_2 doped Si_3N_4 ceramics sintered at 1700 °C could be achieved.

Table 1. Refinement parameters of Ti_3SiC_2 doped Si_3N_4 ceramics.

$\text{Si}_3\text{N}_{4-x}\text{Ti}_3\text{SiC}_2$ vol.%	Weight Fraction			R Factor of Rietveld	Theoretical Density ($\text{g}\cdot\text{cm}^{-3}$)	Densification
	$\beta\text{-Si}_3\text{N}_4$	$\text{C}_{0.3}\text{N}_{0.7}\text{Ti}$	SiC			
$x = 1$	97.3%	0.9%	1.8%	4.76%	3.21	99.26%
$x = 3$	97.1%	0.9%	2.1%	4.55%	3.21	99.89%
$x = 5$	92.8%	4.1%	3.1%	3.46%	3.25	99.92%
$x = 10$	87.3%	7.6%	5.1%	3.42%	3.30	99.73%
$x = 15$	82.3%	11.7%	6.0%	3.47%	3.35	99.98%
$x = 20$	78.4%	14.6%	7.0%	4.07%	3.39	99.79%

Figure 3 shows the micromorphology of polished surface of Si_3N_4 with different volume fractions of Ti_3SiC_2 sintered at 1700°C . Due to the lack of sufficient sintering aids, lots of pores could be observed, and grain growth of $\beta\text{-Si}_3\text{N}_4$ is not complete for monolithic Si_3N_4 ceramic (see Figure 3a). However, the microstructures of $\text{Ti}_3\text{SiC}_2\text{-Si}_3\text{N}_4$ ceramics (see Figure 3b–g) exhibit much more close-grain structure and consist of randomly oriented elongated Si_3N_4 grains which is accordant with XRD results in Figure 2. The average diameters of grains present slight increasing trend from 0.68 to $0.98\ \mu\text{m}$ by quantitative image analysis as the amount of Ti_3SiC_2 increased. Besides, the bright contrasted phase which uniformly embedded in Si_3N_4 matrix could be observed and are inclined to aggregate especially when Ti_3SiC_2 content exceeds 15 vol.%. Furthermore, as shown in Table 2, energy dispersive spectrometer (EDS) at spot A in Figure 3e suggests dominant phase of Si_3N_4 and SiC, which is associated with reaction described by Equation (10). Additional O element may be originated from surface of raw $\alpha\text{-Si}_3\text{N}_4$ powders. Meanwhile, the bright region at spot B is proved to be enriched by Ti according to the EDS results in Table 2. Combined with the results of XRD analysis, it is reasonable to claim that the dispersive bright regions consist of $\text{C}_{0.3}\text{N}_{0.7}\text{Ti}$ and SiC, which are believed to affect the mechanical performance of reaction bonded Si_3N_4 ceramics.

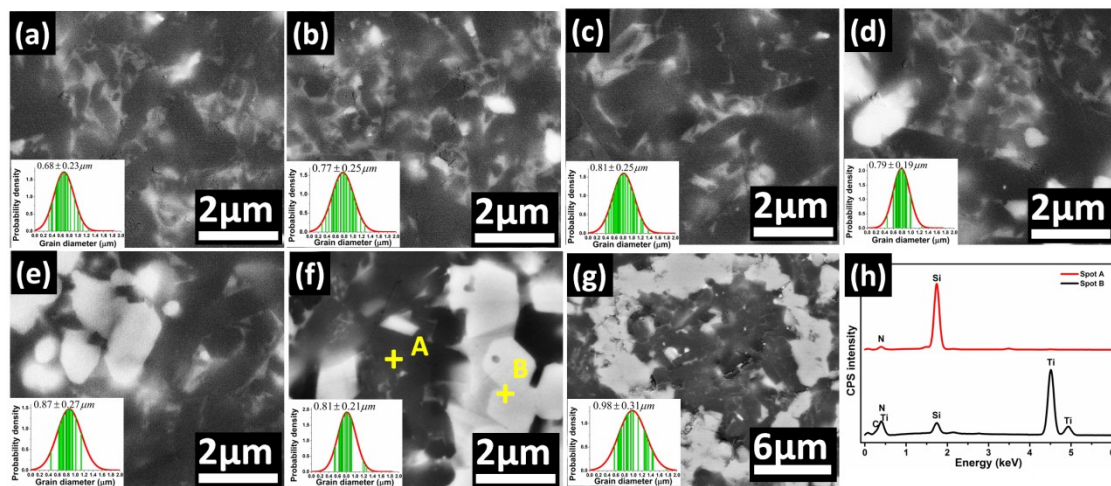


Figure 3. Polished surface of Si_3N_4 ceramics with different content of Ti_3SiC_2 sintered at 1700°C : (a) 5 wt.% Y_2O_3 -2 wt.% Al_2O_3 , (b) 1 vol.% Ti_3SiC_2 , (c) 3 vol.% Ti_3SiC_2 , (d) 5 vol.% Ti_3SiC_2 , (e) 10 vol.% Ti_3SiC_2 , (f) 15 vol.% Ti_3SiC_2 , (g) 20 vol.% Ti_3SiC_2 , (h) EDS spectra at spot A and B.

Table 2. EDS chemical analysis (at.%) at different positions in Figure 3g.

Location	Si	N	O	Ti	C	Possible Phases
Spot A	52.21	35.43	2.04	1.29	9.03	Si_3N_4 , SiC
Spot B	5.10	27.18	-	50.13	17.59	$\text{C}_{0.3}\text{N}_{0.7}\text{Ti}$, SiC

The mechanical properties, including Vickers hardness, flexural strength, and fracture toughness, of dense Si_3N_4 ceramics with different Ti_3SiC_2 content sintered at 1700°C are illustrated in Figure 4.

Clearly, the Vickers hardness of Si_3N_4 ceramics has been upgraded after modification of Ti_3SiC_2 , and presents slight increase compared with that of Si_3N_4 ceramics containing conventional oxides aids. Besides, an obvious enhancement of flexural strength and fracture toughness could be observed. A maximum flexural strength of 795 MPa could be achieved for 5 vol.% Ti_3SiC_2 doped Si_3N_4 composites, which is almost twice that of 7 wt.% $(\text{Y}_2\text{O}_3\text{-Al}_2\text{O}_3)\text{-Si}_3\text{N}_4$ ceramics prepared at the same condition. This enhancement of flexural strength could be attributed to the $\text{C}_{0.3}\text{N}_{0.7}\text{Ti}$ and SiC which originated from reaction bonding between Ti_3SiC_2 and Si_3N_4 [10]. However, further increment of Ti_3SiC_2 content reduces the flexural strength of Si_3N_4 ceramics which may be ascribed to the enhanced residual stresses around grain boundary [58,59]. Please note that this residual stress is believed to result in microcracks and intergranular fracture mode which will be discussed later. Moreover, the fracture toughness of Si_3N_4 composites is also effectively boosted after Ti_3SiC_2 decoration, and reaches maximum value of $6.97 \text{ MPa}\cdot\text{m}^{1/2}$ for 20 vol.% $\text{Ti}_3\text{SiC}_2\text{-Si}_3\text{N}_4$ ceramics which is 37% higher than that of 7 wt.% $(\text{Y}_2\text{O}_3\text{-Al}_2\text{O}_3)\text{-Si}_3\text{N}_4$ ceramics.

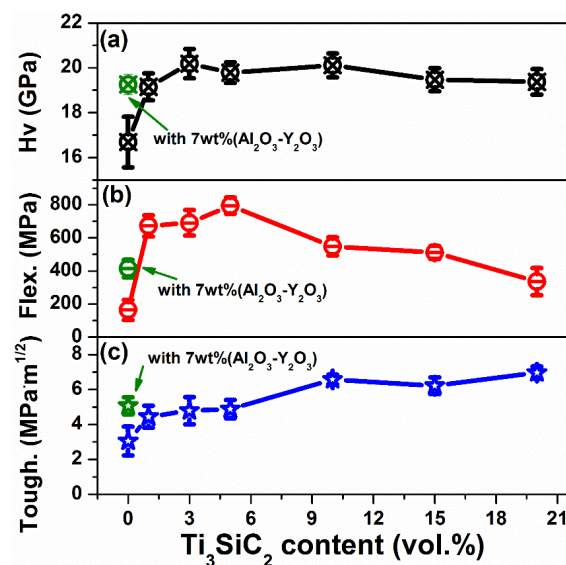


Figure 4. Mechanical properties of Ti_3SiC_2 doped Si_3N_4 ceramics: (a) Vickers hardness; (b) Flexural strength and (c) fracture toughness.

Figure 5 illustrates the typical optical micrographs of the Vickers hardness indents and the induced cracks of Si_3N_4 ceramics with different Ti_3SiC_2 contents, as well as 7 wt.% $(\text{Y}_2\text{O}_3\text{-Al}_2\text{O}_3)$. Clearly, the polished surfaces of Ti_3SiC_2 doped Si_3N_4 ceramics become much smoother than the monolithic Si_3N_4 ceramic which HP sintered at 1700°C , corresponding to the enhancement of densification. Besides, it can be seen that the area of indentation presents no obvious change for Ti_3SiC_2 doped Si_3N_4 ceramics, which is consistent with the stable Vickers hardness. However, the cracks obviously become shorter especially when the Ti_3SiC_2 contents exceed 10 vol.%, which is responsible for the enhancement of fracture toughness.

To illustrate the fracture behaviors and activated toughening mechanisms, micromorphology and crack paths are investigated on cross-sectional fracture surfaces and polished surfaces, respectively. Comparison of typical fracture surfaces between Si_3N_4 doped with $\text{Al}_2\text{O}_3\text{-Y}_2\text{O}_3$ and Ti_3SiC_2 is illustrated in Figure 6. As can be seen from Figure 6a, a small number of pores occur in the $\text{Si}_3\text{N}_4\text{-7 wt.%(Al}_2\text{O}_3\text{-Y}_2\text{O}_3)$ composites, which is harmful for the mechanical performance. In contrast, the $\text{Si}_3\text{N}_4\text{-Ti}_3\text{SiC}_2$ specimen presents a much more close-grain fracture surface owing to the higher density. As marked by red arrows in Figure 6b, large amounts of dimples corresponding to the transgranular fracture could be observed. In addition, this fracture mode is considered to make a dominant contribution to the superior flexural strength of $\text{Si}_3\text{N}_4\text{-Ti}_3\text{SiC}_2$ composites [10]. Besides, as marked by yellow arrows, lots of interface debonding between the Si_3N_4 grains and grain boundary

phase could be observed. This intergranular fracture mode may result from the pullout of elongated β - Si_3N_4 grains, which is believed to make a contribution to the enhancement of overall fracture toughness [60–62].

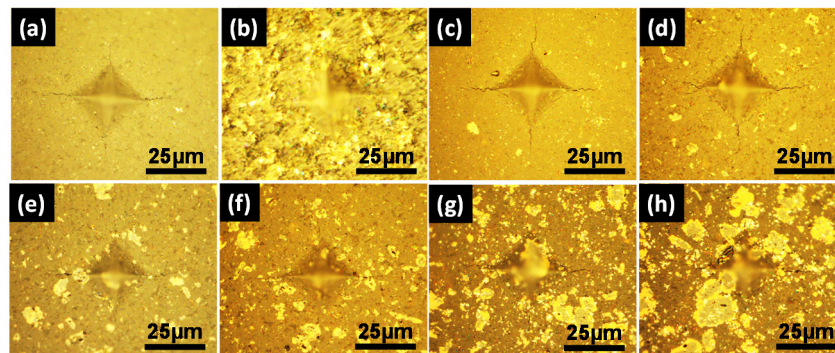


Figure 5. Optical micrographs of the Vickers hardness indents and the induced cracks in (a) Si_3N_4 -7 wt.% (Al_2O_3 - Y_2O_3), (b) Si_3N_4 -3 vol.% Ti_3SiC_2 , (c) Si_3N_4 -5 vol.% Ti_3SiC_2 , (d) Si_3N_4 -10 vol.% Ti_3SiC_2 , (e) Si_3N_4 -15 vol.% Ti_3SiC_2 , (f) Si_3N_4 -20 vol.% Ti_3SiC_2 .

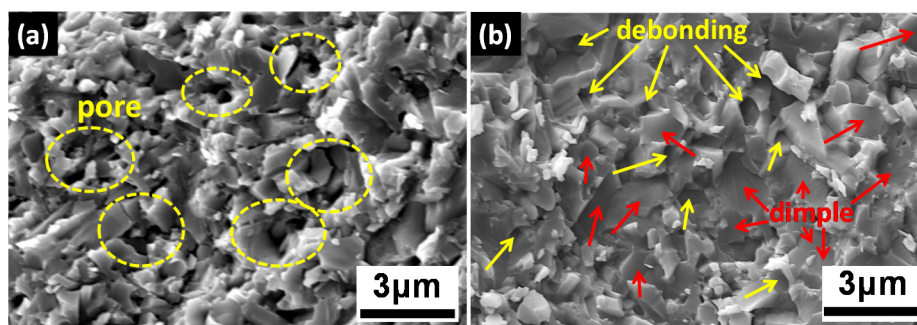


Figure 6. Typical fracture surfaces of Si_3N_4 with (a) 7 wt.% (Al_2O_3 - Y_2O_3), (b) 10 vol.% Ti_3SiC_2 .

Another mechanism of the enhanced fracture toughness of Si_3N_4 - Ti_3SiC_2 composites could be ascribed to the crack branching, deflection, and grain bridging by in situ derived $\text{C}_{0.3}\text{N}_{0.7}\text{Ti}$ and SiC grains embedded in Si_3N_4 matrix, which illustrated in Figure 7. Due to the superior hardness of $\text{C}_{0.3}\text{N}_{0.7}\text{Ti}$ and the thermal mismatch between Si_3N_4 and $\text{C}_{0.3}\text{N}_{0.7}\text{Ti}$, there exists residual stress around $\text{C}_{0.3}\text{N}_{0.7}\text{Ti}$ grains during cooling, giving rise to the microcracks inside composites. When subjected to the external mechanical stress, these microcracks tend to be activated and the propagation path of cracks tends to be split by $\text{C}_{0.3}\text{N}_{0.7}\text{Ti}$ hard-phase and deflected along the interface. Such mechanisms consumed more fracture energy during the crack propagation which leads to crack arrest [63–67].

A comparison of mechanical properties of Si_3N_4 -based ceramics obtained in the present work and selected previous works with conventional oxide aids is shown in Table 3. Clearly, the Vickers, flexural strength, and toughness of Ti_3SiC_2 doped Si_3N_4 ceramics present the same level or even better compared with Si_3N_4 ceramics sintered with oxide aids. Moreover, due to the superior mechanical and thermal properties of in situ formed $\text{C}_{0.3}\text{N}_{0.7}\text{Ti}$ and SiC , Si_3N_4 ceramics obtained in this work are believed to have a significant competitive advantage and to promote the development of Si_3N_4 -based ceramics at high temperatures.

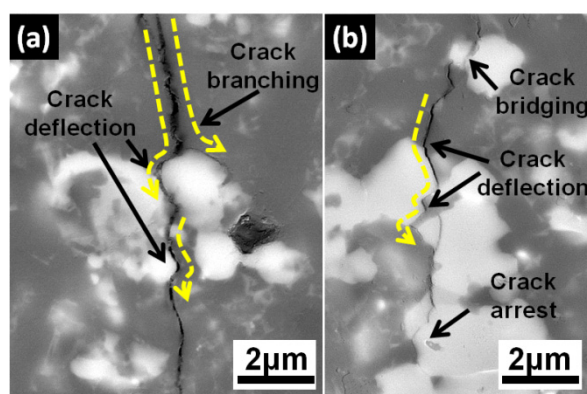


Figure 7. Typical SEM images of crack deflection in Ti_3SiC_2 densified Si_3N_4 composites.

Table 3. Selected results on mechanical properties of Si_3N_4 ceramics by pressure-assisted sintering.

Composition	Sintering Conditions	Vickers Hardness (GPa)	Flexural Strength (MPa)	Fracture Toughness ($\text{MPa}\cdot\text{m}^{1/2}$)	Ref.
$\alpha\text{-Si}_3\text{N}_4 + 4 \text{ wt.}\% \text{ Al}_2\text{O}_3 + 6 \text{ wt.}\% \text{ Y}_2\text{O}_3$	Hot isostatic pressing at 1700 °C, 20 MPa, 3 h	16.4	730	6.5	[27]
$\alpha\text{-Si}_3\text{N}_4 + 5 \text{ wt.}\% \text{ Al}_2\text{O}_3 + 5 \text{ wt.}\% \text{ Y}_2\text{O}_3$	Hot press at 1800 °C, 30 MPa, 1.5 h	16.1	-	5.2	[20]
$\alpha\text{-Si}_3\text{N}_4 + 4 \text{ wt.}\% \text{ Al}_2\text{O}_3 + 6 \text{ wt.}\% \text{ Y}_2\text{O}_3$	Hot press at 1700 °C, 50 MPa, 1.5 h	17.01	-	-	[21]
$\alpha\text{-Si}_3\text{N}_4 + 30 \text{ vol.}\% \beta\text{-Si}_3\text{N}_4$ whiskers + 5 wt.% $\text{Al}_2\text{O}_3 + 5 \text{ wt.}\% \text{ Y}_2\text{O}_3 + 5 \text{ wt.}\% \text{ CeO}_2$	Hot press at 1700 °C, 30 MPa, 30 min	19.0	794	8.6	[22]
$\alpha\text{-Si}_3\text{N}_4 + 4 \text{ wt.}\% \text{ Al}_2\text{O}_3 + 4 \text{ wt.}\% \text{ Y}_2\text{O}_3 + 15 \text{ vol.}\% \text{ SiC}$ whiskers	Hot press at 1800 °C, 30 MPa, 30 min	16	680	6.1	[68]
$\alpha\text{-Si}_3\text{N}_4 + 5 \text{ wt.}\% \text{ Al}_2\text{O}_3 + 4 \text{ wt.}\% \text{ Y}_2\text{O}_3 + 3 \text{ wt.}\% \text{ TiC}$	Gas pressure sintering at 1750 °C, 2 MPa	16.4	475	7.6	[11]
$\alpha\text{-Si}_3\text{N}_4 + 5 \text{ vol.}\% \text{ Ti}_3\text{SiC}_2$	Hot-pressed at 1700 °C for 90 min	19.78	795	4.88	This work
$\alpha\text{-Si}_3\text{N}_4 + 20 \text{ vol.}\% \text{ Ti}_3\text{SiC}_2$	Hot-pressed at 1700 °C for 90 min	20.11	549	6.58	This work

4. Conclusions

In summary, we proposed non-oxide Ti_3SiC_2 (one of typical MAX cermets) as a novel sintering aid to densify Si_3N_4 ceramics with enhanced mechanical properties. A remarkable relative density increment of 20.5% (from 2.58 to 3.11 $\text{g}\cdot\text{cm}^{-3}$) could be observed for 1600 °C hot-press sintered Si_3N_4 ceramics doped with only 5 vol.% Ti_3SiC_2 compared with Si_3N_4 ceramics without aids. Further increase in sintering temperature to 1700 °C brought appreciable consolidation of nearly full dense $\text{Ti}_3\text{SiC}_2\text{-Si}_3\text{N}_4$ ceramics. XRD and EDS investigations demonstrated the formation of $\text{C}_{0.3}\text{N}_{0.7}\text{Ti}$ and SiC which resulted from in situ reaction between Ti_3SiC_2 and Si_3N_4 through diffusion of C and N. The Vickers hardness of Ti_3SiC_2 doped Si_3N_4 ceramics increased slight compared with that of Si_3N_4 ceramics containing conventional oxides aids. Nevertheless, an obvious enhancement of flexural strength and fracture toughness could be observed. A maximum flexural strength of 795 MPa could be obtained for 5 vol.% Ti_3SiC_2 doped Si_3N_4 composites. Moreover, the fracture toughness of Ti_3SiC_2 densified Si_3N_4 composites exhibited a remarkable increase with increasing in volume fraction, and reached maximum value of 6.97 $\text{MPa}\cdot\text{m}^{1/2}$ for 20 vol.% $\text{Ti}_3\text{SiC}_2\text{-Si}_3\text{N}_4$ ceramics. Pull out of elongated Si_3N_4 grains, crack bridging and deflection were demonstrated to promote fracture toughness of Ti_3SiC_2 densified Si_3N_4 composites. With these successes, MAX phase densified Si_3N_4 ceramics with enhanced strength and toughness will be necessary to meet demands of potential future markets for advanced ceramics. Further efforts are encouraged to be devoted to thermal properties investigations of MAX enabled Si_3N_4 composites.

Supplementary Materials: The following are available online at <http://www.mdpi.com/1996-1944/13/6/1428/s1>, Figure S1: Quantitative report of $\text{Si}_3\text{N}_4\text{-1 vol.}\% \text{ Ti}_3\text{SiC}_2$, Figure S2: Quantitative report of $\text{Si}_3\text{N}_4\text{-3 vol.}\% \text{ Ti}_3\text{SiC}_2$, Figure S3: Quantitative report of $\text{Si}_3\text{N}_4\text{-5 vol.}\% \text{ Ti}_3\text{SiC}_2$, Figure S4: Quantitative report of $\text{Si}_3\text{N}_4\text{-10 vol.}\% \text{ Ti}_3\text{SiC}_2$, Figure S5: Quantitative report of $\text{Si}_3\text{N}_4\text{-15 vol.}\% \text{ Ti}_3\text{SiC}_2$, Figure S6: Quantitative report of $\text{Si}_3\text{N}_4\text{-20 vol.}\% \text{ Ti}_3\text{SiC}_2$.

Author Contributions: Supervision, data curation and writing, H.L.; Review and Editing, C.L., Y.L., and L.D.; Funding acquisition, L.D.; Conceptualization and Validation, H.Z. and P.X. All authors have read and agreed to the published version of the manuscript.

Funding: This work was supported by the National Key Research and Development Program of China (Grant No. 2017YFA0204600), the National Natural Science Foundation of China (Grant No. 51802352), the China Postdoctoral Science Foundation (Grant No. 2017M612996).

Acknowledgments: A special acknowledgement is due to Pengfei Liu for his technical assistance in SEM acquisition.

Conflicts of Interest: The authors declare no conflict of interest.

References

1. Xu, W.; Yin, Z.; Yuan, J.; Wang, Z.; Fang, Y. Effects of sintering additives on mechanical properties and microstructure of Si_3N_4 ceramics by microwave sintering. *Mater. Sci. Eng. A* **2017**, *684*, 127–134. [[CrossRef](#)]
2. Kandi, K.K.; Thallapalli, N.; Chilakalapalli, S.P.R. Development of silicon nitride-based ceramic radomes—A review. *Int. J. Appl. Ceram. Technol.* **2015**, *12*, 909–920. [[CrossRef](#)]
3. Nishimura, T.; Xu, X.; Kimoto, K.; Hirosaki, N.; Tanaka, H. Fabrication of silicon nitride nanoceramics—Powder preparation and sintering: A review. *Sci. Technol. Adv. Mater.* **2007**, *8*, 635–643. [[CrossRef](#)]
4. Luo, H.; Tan, Y.; Li, Y.; Xiao, P.; Deng, L.; Zeng, S.; Zhang, G.; Zhang, H.; Zhou, X.; Peng, S. Modeling for high-temperature dielectric behavior of multilayer $\text{Cf}/\text{Si}_3\text{N}_4$ composites in X-band. *J. Eur. Ceram. Soc.* **2017**, *37*, 1961–1968. [[CrossRef](#)]
5. Bucio, T.D.; Bucio, T.D.; Lacava, C.; Clementi, M.; Faneca, J.; Skandalos, I.; Baldycheva, A.; Galli, M.; Debnath, K.; Petropoulos, P.; et al. Silicon nitride photonics for the near-infrared. *IEEE J. Sel. Top. Quantum Electron.* **2020**, *26*, 13. [[CrossRef](#)]
6. Wen, Z.; Zhou, W.; Long, L.; Li, Y. Investigation on electromagnetic wave absorption of $\text{SiCw}/\text{Si}_3\text{N}_4$ composites exposed to short-time oxidation. *J. Nanosci. Nanotechnol.* **2020**, *20*, 1859–1865. [[CrossRef](#)]
7. Kiani, K.M.; Frankis, H.C.; Mbonde, H.M.; Mateman, R.; Leinse, A.; Knights, A.P.; Bradley, J.D. Thulium-doped tellurium oxide waveguide amplifier with 7.6dB net gain on a silicon nitride chip. *Opt. Lett.* **2019**, *44*, 5788–5791. [[CrossRef](#)]
8. Zanocco, M.; Marin, E.; Rondinella, A.; Boschetto, F.; Horiguchi, S.; Zhu, W.; McEntire, B.J.; Bock, R.M.; Bal, B.S.; Pezzotti, G. The role of nitrogen off-stoichiometry in the osteogenic behavior of silicon nitride bioceramics. *Mater. Sci. Eng. C Mater. Biol. Appl.* **2019**, *105*, 8. [[CrossRef](#)]
9. Nikonam, M.R.; Pugh, M.D.; Drew, R.A.L. Microstructural evolution mechanism of porous reaction bonded silicon nitride ceramics heat-treated in two powder beds. *Ceram. Int.* **2019**, *45*, 21986–21997. [[CrossRef](#)]
10. Liu, J.; Yang, J.; Zhu, S.; Cheng, J.; Yu, Y.; Qiao, Z.; Liu, W. Temperature-driven wear behavior of Si_3N_4 -based ceramic reinforced by in situ formed $\text{TiC}_{0.3}\text{N}_{0.7}$ particles. *J. Am. Ceram. Soc.* **2019**, *102*, 4333–4343. [[CrossRef](#)]
11. Ye, C.; Yue, X.; Ru, H.; Long, H.; Gong, X. Effect of addition of micron-sized TiC particles on mechanical properties of Si_3N_4 matrix composites. *J. Alloy. Compd.* **2017**, *709*, 165–171. [[CrossRef](#)]
12. Bocanegra-Bernal, M.H.; Matovic, B. Mechanical properties of silicon nitride-based ceramics and its use in structural applications at high temperatures. *Mater. Sci. Eng. A* **2010**, *527*, 1314–1338. [[CrossRef](#)]
13. Klemm, H. Silicon nitride for high-temperature applications. *J. Am. Ceram. Soc.* **2010**, *93*, 1501–1522. [[CrossRef](#)]
14. Shi, C.; Zhu, Y.; Qian, H.; Lu, L. Fabrication of silicon nitride fiber-PMMA composite through free radical polymerization in batch. *Mater. Res. Bull.* **2014**, *51*, 161–166. [[CrossRef](#)]
15. Eblagon, F.; Ehrle, B.; Graule, T.; Kuebler, J. Development of silicon nitride/silicon carbide composites for wood-cutting tools. *J. Eur. Ceram. Soc.* **2007**, *27*, 419–428. [[CrossRef](#)]
16. Buzbee, M.; Lombardo, D.; Zhan, Q.; Hendrickson, J.; Sarangan, A.; Agha, I. Silicon nitride on-silicon 3-dimensional photonic circuits for integrated photodetection. In *Advanced Photonics 2016 (IPR, NOMA, Sensors, Networks, SPPCom, SOF)*; Optical Society of America: Vancouver, BC, Canada, 2016.
17. Xie, W.; Stöferle, T.; Raino, G.; Aubert, T.; Bisschop, S.; Zhu, Y.; Van Thourhout, D. On-chip integrated quantum-dot-silicon-nitride microdisk lasers. *Adv. Mater.* **2017**, *29*, 1604866-6. [[CrossRef](#)]

18. Nishiyama, N.; Ishikawa, R.; Ohfuji, H.; Marquardt, H.; Kurnosov, A.; Taniguchi, T.; Kulik, E. Transparent polycrystalline cubic silicon nitride. *Sci. Rep.* **2017**, *7*, 44755. [[CrossRef](#)]
19. Capelle, T.; Tsaturyan, Y.; Barg, A.; Schliesser, A. Polarimetric analysis of stress anisotropy in nanomechanical silicon nitride resonators. *Appl. Phys. Lett.* **2017**, *110*, 181106. [[CrossRef](#)]
20. Yu, J.-J.; Guo, W.M.; Sun, S.K.; Lin, H.T.; Wang, C.Y. Graded Si₃N₄ ceramics with hard surface and tough core by two-step hot pressing. *Ceram. Int.* **2017**, *43*, 7948–7950. [[CrossRef](#)]
21. Balázsi, C.; Fogarassy, Z.; Tapasztó, O.; Kailer, A.; Schröder, C.; Parchoviansky, M.; Balázsi, K. Si₃N₄/graphene nanocomposites for tribological application in aqueous environments prepared by attritor milling and hot pressing. *J. Eur. Ceram. Soc.* **2017**, *37*, 3797–3804. [[CrossRef](#)]
22. Xing, H.; Liu, B.; Sun, J.; Zou, B. Mechanical properties of Si₃N₄ ceramics from an in-situ synthesized α-Si₃N₄/β-Si₃N₄ composite powder. *Ceram. Int.* **2017**, *43*, 2150–2154. [[CrossRef](#)]
23. Liang, H.; Zeng, Y.; Zuo, K.; Xia, Y.; Yao, D.; Yin, J. Mechanical properties and thermal conductivity of Si₃N₄ ceramics with YF₃ and MgO as sintering additives. *Ceram. Int.* **2016**, *42*, 15679–15686. [[CrossRef](#)]
24. Li, S.; Xie, Z.; Xue, W.; Luo, X.; An, L. Sintering of high-performance silicon nitride ceramics under vibratory pressure. *J. Am. Ceram. Soc.* **2015**, *98*, 698–701. [[CrossRef](#)]
25. Mikijelj, B.; Nawaz, Z.; Kruzic, J.J.; Idrobo, J.; Swab, J.J.; Özcoban, H.; Liu, Y. Intergranular nanostructure effects on strength and toughness of Si₃N₄. *J. Am. Ceram. Soc.* **2015**, *98*, 1650–1657. [[CrossRef](#)]
26. Zhou, M.Y.; Zhong, J.; Zhao, J.; Rodrigo, D.; Cheng, Y.B. Microstructures and properties of Si₃N₄/TiN composites sintered by hot pressing and spark plasma sintering. *Mater. Res. Bull.* **2013**, *48*, 1927–1933. [[CrossRef](#)]
27. Kovalčíková, A.; Balko, J.; Balázsi, C.; Hvizdoš, P.; Dusza, J. Influence of hBN content on mechanical and tribological properties of Si₃N₄/BN ceramic composites. *J. Eur. Ceram. Soc.* **2014**, *34*, 3319–3328. [[CrossRef](#)]
28. Shen, Z.; Zhao, Z.; Peng, H.; Nygren, M. Formation of tough interlocking microstructures in silicon nitride ceramics by dynamic ripening. *Nature* **2002**, *417*, 266. [[CrossRef](#)]
29. Ahmad, N.; Sueyoshi, H. Microstructure and mechanical properties of silicon nitride-titanium nitride composites prepared by spark plasma sintering. *Mater. Res. Bull.* **2011**, *46*, 460–463. [[CrossRef](#)]
30. Chockalingam, S.; Earl, D.A. Mechanical properties of 2.45GHz microwave sintered Si₃N₄-Y₂O₃-MgO-ZrO₂ system. *J. Eur. Ceram. Soc.* **2009**, *29*, 2037–2043. [[CrossRef](#)]
31. Shibata, N.; Pennycook, S.J.; Gosnell, T.R.; Painter, G.S.; Shelton, W.A.; Becher, P.F. Observation of rare-earth segregation in silicon nitride ceramics at subnanometre dimensions. *Nature* **2004**, *428*, 730–733. [[CrossRef](#)]
32. Riley, F.L. Silicon nitride and related materials. *J. Am. Ceram. Soc.* **2010**, *83*, 245–265. [[CrossRef](#)]
33. Lojanová, S.; Tatarko, P.; Chlup, Z.; Hnatko, M.; Dusza, J.; Lenčes, Z.; Šajgalík, P. Rare-earth element doped Si₃N₄/SiC micro/nano-composites—RT and HT mechanical properties. *J. Eur. Ceram. Soc.* **2010**, *30*, 1931–1944. [[CrossRef](#)]
34. Guo, W.-M.; Wu, L.X.; Ma, T.; You, Y.; Lin, H.T. Rapid fabrication of Si₃N₄ ceramics by reaction-bonding and pressureless sintering. *J. Eur. Ceram. Soc.* **2016**, *36*, 3919–3924. [[CrossRef](#)]
35. Luo, H.; Xiao, P.; Hong, W. Dielectric behavior of laminate-structure Cf/Si₃N₄ composites in X-band. *Appl. Phys. Lett.* **2014**, *105*, 172903. [[CrossRef](#)]
36. Park, H.; Kim, H.-E.; Niihara, K. Microstructural evolution and mechanical properties of Si₃N₄ with Yb₂O₃ as a sintering additive. *J. Am. Ceram. Soc.* **1997**, *80*, 750–756. [[CrossRef](#)]
37. Barsoum, M.W. The MN+1AX_n phases: A new class of solids. *Prog. Solid State Chem.* **2000**, *28*, 201–281. [[CrossRef](#)]
38. Sun, Z.M. Progress in research and development on MAX phases: A family of layered ternary compounds. *Int. Mater. Rev.* **2011**, *56*, 143–166. [[CrossRef](#)]
39. Tzenov, N.V.; Barsoum, M.W. Synthesis and Characterization of Ti₃AlC₂. *J. Am. Ceram. Soc.* **2010**, *83*, 825–832. [[CrossRef](#)]
40. Zhou, W.; Mei, B.; Zhu, J. Rapid synthesis of Ti₃AlC₂/TiB₂ composites by the spark plasma sintering (SPS) technique. *Ceram. Int.* **2009**, *35*, 3507–3510.
41. Li, M.; Li, C.; Li, J.; Zhou, Y. Oxidation behavior of a Ti₃AlC₂/TiB₂ composite at 1000–1400 °C in Air. *J. Am. Ceram. Soc.* **2010**, *93*, 554–560. [[CrossRef](#)]
42. Li, C.; Li, M.; Zhou, Y.; Zhang, J.; He, L. In situ synthesis and properties of Ti₃AlC₂/TiB₂ composites. *J. Am. Ceram. Soc.* **2007**, *90*, 3615–3620. [[CrossRef](#)]

43. Zhu, J.; Ye, L.; Wang, F. Fabrication of $\text{Ti}_3\text{AlC}_2/\text{Al}_2\text{O}_3$ nanocomposite by a novel method. *Sci. Sinter.* **2011**, *43*, 289–294. [[CrossRef](#)]
44. Yeh, C.L.; Kuo, C.W.; Chu, Y.C. Formation of $\text{Ti}_3\text{AlC}_2/\text{Al}_2\text{O}_3$ and $\text{Ti}_3\text{AlC}_2/\text{Al}_2\text{O}_3$ composites by combustion synthesis in Ti–Al–C– TiO_2 systems. *J. Alloy. Compd.* **2010**, *494*, 132–136. [[CrossRef](#)]
45. Liu, Y.; Luo, F.; Su, J.; Zhou, W.; Zhu, D. Mechanical, dielectric, and microwave-absorption properties of alumina ceramic containing dispersed Ti_3SiC_2 . *J. Electron. Mater.* **2015**, *44*, 867–873. [[CrossRef](#)]
46. Tan, Y.Q.; Tan, Y.Q.; Chen, C.; Li, F.Z.; Zhang, H.B.; Zhang, G.J.; Peng, S.M. Enhancement of sinterability and mechanical properties of B4C ceramics using Ti_3AlC_2 as a sintering aid. *RSC Adv.* **2015**, *5*, 76309–76314. [[CrossRef](#)]
47. Tan, Y.; Luo, H.; Zhang, H.; Zhou, X.; Peng, S. Lightweight graphene nanoplatelet/boron carbide composite with high EMI shielding effectiveness. *AIP Adv.* **2016**, *6*, 035208. [[CrossRef](#)]
48. Tan, Y.; Luo, H.; Zhang, H.; Zhou, X.; Peng, S. Fabrication of toughened B4C composites with high electrical conductivity using MAX phase as a novel sintering aid. *Ceram. Int.* **2016**, *42*, 7347–7352. [[CrossRef](#)]
49. Tan, Y.; Luo, H.; Zhang, H.; Peng, S. Graphene nanoplatelet reinforced boron carbide composites with high electrical and thermal conductivity. *J. Eur. Ceram. Soc.* **2016**, *36*, 2679–2687. [[CrossRef](#)]
50. Tan, Y.; Zhang, H.; Peng, S. Electrically conductive graphene nanoplatelet/boron carbide composites with high hardness and toughness. *Scr. Mater.* **2016**, *114*, 98–102. [[CrossRef](#)]
51. Zhou, Y.; Hyuga, H.; Kusano, D.; Yoshizawa, Y.I.; Ohji, T.; Hirao, K. Development of high-thermal-conductivity silicon nitride ceramics. *J. Asian Ceram. Soc.* **2015**. [[CrossRef](#)]
52. Clarke, D.R. Densification of silicon nitride: Effect of chlorine impurities. *J. Am. Ceram. Soc.* **1982**, *65*. [[CrossRef](#)]
53. Wu, E.; Riley, D.P.; Kisi, E.H.; Smith, R.I. In situ neutron powder diffraction study of Ti_3SiC_2 synthesis. *J. Am. Ceram. Soc.* **2004**, *84*, 2281–2288. [[CrossRef](#)]
54. Racault, C.; Langlais, F.; Naslain, R. Solid-state synthesis and characterization of the ternary phase Ti_3SiC_2 . *J. Mater. Sci.* **1994**, *29*, 3384–3392. [[CrossRef](#)]
55. Mitomo, M.; Uenosono, S. Microstructural development during gas-pressure sintering of α -silicon nitride. *J. Am. Ceram. Soc.* **1992**, *75*, 103–107. [[CrossRef](#)]
56. Biswas, S.K.; Riley, F.L. Gas pressure sintering of silicon nitride—Current status. *Mater. Chem. Phys.* **2001**, *67*, 175–179. [[CrossRef](#)]
57. Ziegler, G.; Heinrich, J.; Wötting, G. Relationships between processing, microstructure and properties of dense and reaction-bonded silicon nitride. *J. Mater. Sci.* **1987**, *22*, 3041–3086. [[CrossRef](#)]
58. Pezzotta, M.; Zhang, Z.L. Effect of thermal mismatch induced residual stresses on grain boundary microcracking of titanium diboride ceramics. *J. Mater. Sci.* **2010**, *45*, 382–391. [[CrossRef](#)]
59. Ma, H.-B.; Ma, H.B.; Zhang, G.J.; Liu, H.L.; Liu, J.X.; Lu, Y.; Xu, F.F. Effect of WC or ZrC addition on thermal residual stresses in ZrB_2SiC ceramics. *Mater. Des.* **2016**, *110*, 340–345. [[CrossRef](#)]
60. Iizuka, T.; Muraio, T.; Yamamoto, H.; Kita, H. Microstructures and Properties of Mo_5Si_3 -Particle-Reinforced Si_3N_4 -Matrix Composites. *J. Am. Ceram. Soc.* **2002**, *85*, 954–960. [[CrossRef](#)]
61. Fukasawa, T.; Goto, Y. Mechanical properties Of Si_3N_4 ceramics reinforced with SiC whiskers and SiC platelets. *J. Mater. Sci.* **1998**, *33*, 1647–1651. [[CrossRef](#)]
62. Hirosaki, N.; Akimune, Y.; Mitomo, M. Effect of grain growth of β -silicon nitride on strength, weibull modulus, and fracture toughness. *J. Am. Ceram. Soc.* **1993**, *76*, 1892–1894. [[CrossRef](#)]
63. Kvetková, L.; Duszová, A.; Hvizdoš, P.; Dusza, J.; Kun, P.; Balázsi, C. Fracture toughness and toughening mechanisms in graphene platelet reinforced Si_3N_4 composites. *Scr. Mater.* **2012**, *66*, 793–796. [[CrossRef](#)]
64. Mishnaevsky, L.; Lippmann, N.; Schmauder, S. Computational modeling of crack propagation in real microstructures of steels and virtual testing of artificially designed materials. *Int. J. Fract.* **2003**, *120*, 581–600. [[CrossRef](#)]
65. Baik, D.S.; No, K.S.; Chun, J.S.S.; Yoon, Y.J. Mechanical properties of mica glass-ceramics. *J. Am. Ceram. Soc.* **1995**, *78*, 1217–1222. [[CrossRef](#)]
66. Faber, K.T.; Evans, A.G. Intergranular crack-deflection toughening in silicon carbide. *J. Am. Ceram. Soc.* **1983**, *66*. [[CrossRef](#)]

67. Nisar, A.; Balani, K. Synergistic reinforcement of carbon nanotubes and silicon carbide for toughening tantalum carbide based ultrahigh temperature ceramic. *J. Mater. Res.* **2016**. [[CrossRef](#)]
68. Wu, W.; Gui, J.; Wei, S.; Xue, W.; Xie, Z. Si₃N₄-SiCw composites as structural materials for cryogenic application. *J. Eur. Ceram. Soc.* **2016**, *36*, 2667–2672. [[CrossRef](#)]



© 2020 by the authors. Licensee MDPI, Basel, Switzerland. This article is an open access article distributed under the terms and conditions of the Creative Commons Attribution (CC BY) license (<http://creativecommons.org/licenses/by/4.0/>).